

Article

Multi-Temporal Land Cover Classification with Sequential Recurrent Encoders

Marc Rußwurm ¹  and **Marco Körner** ¹ ¹ {marc.russwurm, marco.koerner}@tum.de; Technical University of Munich, Arcisstraße 21, 80333 Munich

* Correspondence: marc.russwurm@tum.de; Tel.: +49-172-81-70-121

submitted to IJGI: January 22nd 2018

Abstract: *Earth observation (EO) sensors deliver data with daily or weekly temporal resolution. Most land use and land cover classification (LULC) approaches, however, expect cloud-free and mono-temporal observations. The increasing temporal capabilities of today's sensors enables the use of temporal, along with spectral and spatial features. Domains, such as speech recognition or neural machine translation, work with inherently temporal data and, today, achieve impressive results using sequential encoder-decoder structures. Inspired by these sequence-to-sequence models, we adapt an encoder structure with convolutional recurrent layers in order to approximate a phenological model for vegetation classes based on a temporal sequence of *Sentinel 2* (S2) images. In our experiments, we visualize internal activations over a sequence of cloudy and non-cloudy images and find several recurrent cells, which reduce the input activity for cloudy observations. Hence, we assume that our network has learned cloud-filtering schemes solely from input data, which could alleviate the need for tedious cloud-filtering as a preprocessing step for many EO approaches. Moreover, using unfiltered temporal series of *top-of-atmosphere (TOA)* reflectance data, we achieved in our experiments state-of-the-art classification accuracies on a large number of crop classes with minimal preprocessing compared to other classification approaches.*

Keywords: deep learning; multi-temporal classification; land use and land cover classification; recurrent networks; sequence encoder; crop classification; sequence-to-sequence; sentinel 2

1. Introduction

Land use and land cover classification (LULC) has been in focus of *earth observation (EO)* since first air- and spaceborne sensors provided data. For this purpose, optical sensors sample, in repeated intervals, the spectral reflectivity of objects on the earth's surface at a spatial grid. Hence, LULC classes can be characterized by spectral, spatial, and also temporal features which can be utilized by classification approaches to varying degrees. Today, most classification tasks focus on spatial and spectral features, while utilizing the temporal domain has previously remained challenging. This is mostly due to limitations on data availability, the cost of data acquisition, infrastructural challenges regarding data storage and processing, and the complexity of model design and feature extraction over multiple timeframes.

Some LULC classes, such as urban structures, are mostly invariant to temporal changes and, hence, are suitable for mono-temporal approaches. Others, predominantly vegetation-related classes, change their spectral reflectivity based on biochemical processes, which are initiated by *phenological* events, related to the type of vegetation, and environmental conditions. In the last decades, these vegetation-characteristic phenological transitions have been utilized for crop yield prediction and, to some extent, for classification [1,2]. However, to circumvent previously mentioned challenges, the dimensionality of spectral bands was often compressed by calculating task-specific indices, such as *normalized difference vegetation index (NDVI)*, *normalized difference water index (NDWI)*, or the *enhanced vegetation index (EVI)*.

Today, most of these limitations regarding temporal data are alleviated by technological advances. The data of multi-spectral earth observation sensors is, with reasonable spatial and temporal resolution, available at no cost. Compared to previous decades, new services inexpensively provide imagery of high temporal and spatial resolution with a moderate number of spectral bands. The cost of data storage has decreased and data transmission has become sufficiently fast, allowing for gathering and processing all available images over a large area and multiple years. And finally, new advances in machine learning, accompanied by GPU accelerated hardware, have made learning complex functional relationships, solely from provided data, possible.

Since data is available and processing is feasible at large-scale, the temporal domain should be exploited for EO approaches. However, due to the common focus on spatial and spectral features, suitable processing techniques are in high demand, which utilize all available temporal information and are applicable at reasonable complexity. Other domains, such as machine translation [3], text summarization [4–6], or speech recognition [7,8], handle sequential data naturally. These domains have popularized sequence-to-sequence learning, which encodes a variable-length input sequence to an intermediate representation. This representation is then decoded to a variable-length output sequence. From this concept, we adopt the sequential encoder structure for this work, as we will describe later in Section 3.1. With the proposed network, we are able to extract characteristic temporal features with a straightforward, two-layer structure.

Thus, the main contributions of this work are

- i) the adaptation of sequence encoders from the field of sequence-to-sequence learning to EO,
- ii) a visualization of internal gate activations on a sequence of EO observations, and
- iii) the application of crop classification over two growth seasons.

2. Related Work

As we aim to apply our network to vegetation classes, we first introduce common crop classification approaches, to which we will compare our results in Section 6. Then, we motivate data-driven learning models and cover the latest work on recurrent network structures in the EO domain.

Many remote sensing approaches have achieved good classification accuracies for multi-temporal crop data by using multiple preprocessing steps in order to improve feature separability. Common methods are atmospheric correction [9–13], calculation of vegetation indices [9–13], or the extraction of sophisticated phenological features [12]. Additionally, some approaches utilize expert knowledge, for instance, by introducing additional agro-meteorological data [9], by selecting suitable observation dates for the target crop-classes [13], or by determining rules for classification [10]. Pixel-based [9,12] and object-based [10,11,13] approaches have been proposed, with the former being generally more susceptible to salt-and-pepper noise and the latter requiring an additional segmentation preprocessing step. Commonly, *decision trees* (DTs) [9,10,13] or *random forests* (RFs) [11,12] are used as classifiers, of which the classification rules are sometimes aided by additional expert knowledge [10].

These traditional approaches generally trade procedural complexity and the use of region-specific expert knowledge for good classification accuracies in the respective *areas of interest* (AOIs). Despite this, these approaches are, in general, difficult to apply to other regions. Furthermore, the processing structure requires supervision to a varying degree (e.g., product selection, visual image inspection, parameter tuning), which impedes application at larger scales.

Today, we experience a change in paradigm: Away from the design of physically interpretable, human-understandable models, which require task-specific expert knowledge, towards data-driven models, which are encoded in internal weight parameters and derived solely from observations. In that regard, *hidden Markov models* (HMMs) [14] or *conditional random fields* (CRFs) [15] have shown good classification accuracies with multi-temporal data. However, the underlying *Markov property* limits long-term learning capabilities, such as multi-year dependencies, as these approaches assume that the present state does only depend on the current input and *one* previous state.

Table 1. Update formulas of the convolutional variants of standard *recurrent neural networks (RNNs)*, *long short-term memory (LSTM)* cells and *gated recurrent units (GRUs)*. A convolution between matrices a and b is denoted by $a * b$, element-wise multiplication by the *Hadamard operator* $a \odot b$, and concatenation of on the last dimension is marked by $[a \| b]$. The activation functions sigmoid σ and tangens hyperbolicus $\tanh(x)$ are used for non-linear scaling.

Gate	Variant			
		RNN	LSTM [25]	GRU [26]
Update	$h_t \leftarrow x_t, h_{t-1}$	$h_t, c_t \leftarrow x_t, h_{t-1}, c_{t-1}$		$h_t \leftarrow x_t, h_{t-1}$
Forget/Reset		$f_t \leftarrow \sigma([x_t \ h_{t-1}] * W_f + 1)$		$r_t \leftarrow \sigma([x_t \ h_{t-1}] * W_r)$
Insert		$i_t \leftarrow \sigma([x_t \ h_{t-1}] * W_i)$ $j_t \leftarrow \sigma([x_t \ h_{t-1}] * W_j)$		$u_t \leftarrow \sigma([x_t \ h_{t-1}] * W_u)$
Output		$o_t \leftarrow \sigma([x_t \ h_{t-1}] * W_o)$		$\tilde{h}_t \leftarrow [x_t \ r_t \odot h_{t-1}] * W_{\tilde{h}}$
State		$c_t \leftarrow c_{t-1} \odot f_t + i_t \odot j_t$		
Output	$h_t \leftarrow \sigma(W * \tilde{x})$	$h_t \leftarrow o_t \odot \tanh(c_t)$		$h_t \leftarrow u_t \odot h_{t-1} + (1 - u_t) \odot \tanh(\tilde{h}_t)$

In latest approaches, *deep learning* methods have proven particularly beneficial for modeling physical relationship, which are complicated, cannot be generalized, or are not well understood [16]. Thus, deep learning is potentially well suited to approximate models of phenological changes, since these relations depend on complex internal biochemical processes of which only the change of surface reflectivity can be observed by EO sensors. Hence, a purely data-driven approach might alleviate the need to manually design a functionally model for this complex relationship. However, caution is required, as external, and non class-relevant factors, such as seasonal weather or observation configurations, are potentially incorporated into the model, which might remain undetected if these factors constantly bias the dataset.

In remote sensing, *convolutional networks* have gained increasing popularity for mono-temporal observation tasks [17–20]. However, for sequential tasks, recurrent network architectures are generally better suited, as these structures provide an iterative framework to process sequential information. Thus, similar to our methodology, recent approaches utilize recurrent architectures for change detection [21], identification of sea level anomalies [22], and land cover classification [23]. For multi-seasonal, long-term dependencies, Jia *et al.* [21] proposed a new cell architecture, which maintains two separate cell states for single- and multi-seasonal long-term dependencies. However, the calculation of an additional cell state requires more weights, which may prolongate training and require more training samples.

In previous work, we have experimented with recurrent networks for crop classification [24] and achieved promising results. Based on this work, we propose a network structure using convolutional recurrent layers and the aforementioned adaptation of a *many-to-one* classification scheme with sequence encoders.

3. Methodology

Section 3.1 incrementally introduces the concepts of *artificial neural networks (ANNs)*, *feed-forward networks (FNNs)*, and *recurrent neural networks (RNNs)* and illustrates the use of RNNs in sequence-to-sequence learning. In this context, we then describe details of the proposed network structure in Section 3.2.

3.1. Network Architectures and Sequential Encoders

ANNs approximate a function $\hat{y} = f(x; W)$ of outputs \hat{y} (e.g., *class labels*) from *input data* x given a large set of *weights* W . This approximation is commonly referred to as *inference* phase. ANNs are

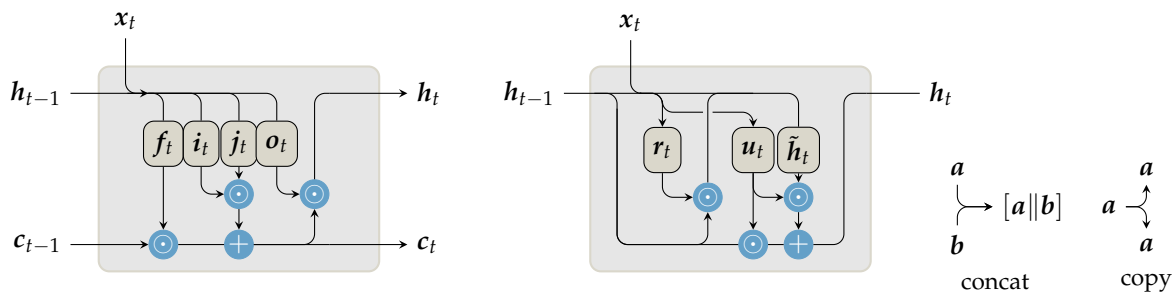


Figure 1. Schematic illustration of long short-term memory (LSTM) and gated recurrent unit (GRU) cells analog to the cell definitions at Table 1. The cell output h_t is calculated via internal gates and based on the current input x_t combined with prior context information h_{t-1} , c_{t-1} . LSTM cells are designed to separately accommodate *long-term* context in the internal cell state c_{t-1} , from *short-term* context h_{t-1} . GRU cells combine all context information in a single, but more sophisticated output h_t .

usually composed of multiple cascaded layers with *hidden* vectors h as intermediate layer outputs. Due to the original analogy to the biological neural cortex, single elements in these vectors are often referred to as *neurons*. In end-to-end learning, the quality of the approximation \hat{y} with respect to ground truth y is determined by the *loss function* $L(\hat{y}, y)$. Based on this loss, gradients are *back-propagated* through the ANN and adjust network weights W at each *training* step.

Popular feed-forward networks often utilize *convolutional* or *fully-connected* layers, which process the input vector once. This is realized by an affine transformation (fully-connected) $h = \sigma(Wx)$ or a convolution $h = \sigma(W * x)$ followed by an element-wise, non-linear transformation $\sigma : \mathbb{R} \mapsto \mathbb{R}$.

However, domains, like translation [3], text summarization [4–6], or speech recognition [7,8], formulate input vectors naturally as a sequence of observations $x = \{x_0, \dots, x_T\}$. At these fields, context information from previous and next sequence elements benefits the performance of the model to a large degree.

To utilize this information, recurrent neural network (RNN) layers are commonly used, in which at time t the hidden layer output h_t is determined by current input x_t in combination with the previous output h_{t-1} . This update is performed iteratively and enables RNNs to theoretically simulate arbitrary procedures [27], since these networks are *Turing complete* [28]. The standard RNN variant performs the update step $h_t = \sigma(W\tilde{x})$ by affine transformation of the concatenated vector $\tilde{x} = [x_t \parallel h_{t-1}]$ followed by a non-linearity σ . Consequently, the internal weight matrix is multiplied multiple times, which essentially raises it to a high power [29]. At gradient back-propagation, this iterative matrix multiplication leads to *vanishing* and *exploding gradients* [30,31]. While exploding gradients can be avoided by *gradient clipping*, vanishing gradients impede the training of standard RNNs for tasks which require the extraction of long-term features. This issue has been addressed by Hochreiter and Schmidhuber [25] who introduced an internal *state* vector c_t and additional gates in LSTM cells, which control the gradient propagation through time and enable *long-term* learning. At each observation time t , three gates control the degree of stored information in c_t . The *forget gate* f_t decreases previously stored information by element-wise multiplication $c_{t-1} \odot f_t$. New information is added by the multiplicative combination of *input gate* i_t and *modulation gate* j_t . A fourth *output gate* o_t combines long-term cell state information c_{t-1} with short-term information $[x_t \parallel h_{t-1}]$. Illustrations of the internal calculation can be seen at Figure 1, and the mathematical relations are shown at Table 1. Besides LSTMs, gated recurrent units (GRUs) [26] have gained increasing popularity, as these cells achieve similar accuracies to LSTMs with fewer trainable parameters. Instead of separate vectors for long and short-term memory, GRUs formulate a single, but more sophisticated output vector.

As previously introduced, recurrent layers provide a *many-to-many* relation by generating an output vector at each observation h_t given previous context h_{t-1} and c_{t-1} . However, encoding

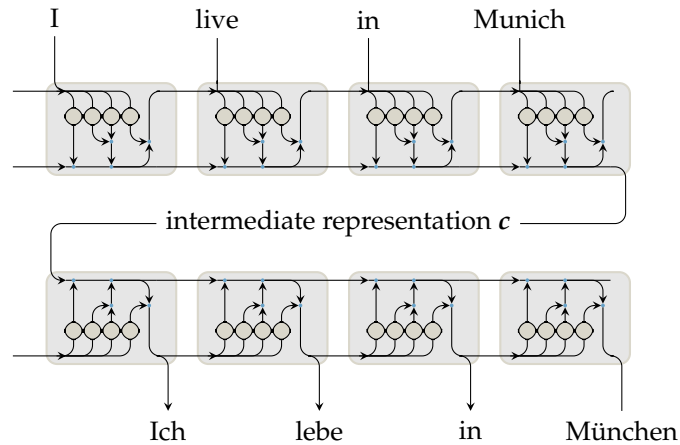


Figure 2. Basic conceptual illustration of a sequence-to-sequence, encoder-decoder network without attention mechanism [7], as used in neural translation tasks. First, a recurrent neural network (RNN) variant (e.g., LSTM, or GRU) encodes a variable-length input sequence to a fixed-size representation c . A second decoder structure produces the desired variable-length output sequence.

information of the entire sequence in a *many-to-one* relation is favored in many applications. Following this idea, *sequence-to-sequence* learning has popularized using the final cell state vector c_T as the representation of the entire input sequence. *Sequence-to-sequence* networks are encoding-decoding structures, which first encode an input sequence of variable length to an intermediate state representation c of fixed size. Then, this representation is decoded to a variable length output sequence. Figure 2 shows a conceptual example of a sequence-to-sequence model with LSTM cells for translation tasks. Further developments in this domain include *attention schemes*, which provide additional connections between encoder and decoder and have shown to improve translation performance at longer sequence lengths [3].

In many sequential applications, the common input form is of $x_t \in \mathbb{R}^d$ with a given *depth* d . The output vectors $h_t \in \mathbb{R}^r$ are computed by matrix multiplication with internal weights $W \in \mathbb{R}^{(r+d) \times r}$ with r representing the number of recurrent cells. However other fields, such as image processing, commonly handle raster data $x_t \in \mathbb{R}^{h \times w \times d}$ of specific *width* w , *height* h , and *depth* d . To account for neighborhood relationships and to circumvent the increasing complexity, convolutional variants of LSTMs [32] and GRUs have been introduced, which have also found application in sequence-to-sequence learning [33].

3.2. Approach

In this work, we employ a bidirectional sequential encoder for the task of multi-temporal land cover classification. As earth observation data is gathered in a periodic manner, many observations of the same area at consecutive times are available, which can contribute to the classification decision. Hence, the encoding of a multi-temporal image sequence to a fixed-length state representation is an elegant way to condense the available temporal dimension to a feature map which contains information of the entire temporal series. Additionally, many optical observations are covered by clouds, which—in traditionally approaches—have to be masked out using additional cloud-classification methods. By introducing raw image sequences to a recurrent encoder, the network can potentially learn that cloudy observations do not contribute to the classification task. Thus, by theory, the network should internalize a cloud-filtering scheme based on provided data in an end-to-end fashion.

Figure 3 illustrates schematically the proposed network structure. The input image sequence $x = \{x_t, \dots, x_T\}$ of observations $x \in \mathbb{R}^{h \times w \times d}$ is passed to gated recurrent layers at each observation time t . The index T denotes the maximum length of the sequence and d the input feature depth. In practice, sequence lengths are often shorter than T depending on availability of image at the respective acquisition rows. For this reason, the observations outside of the effective sequence are padded with

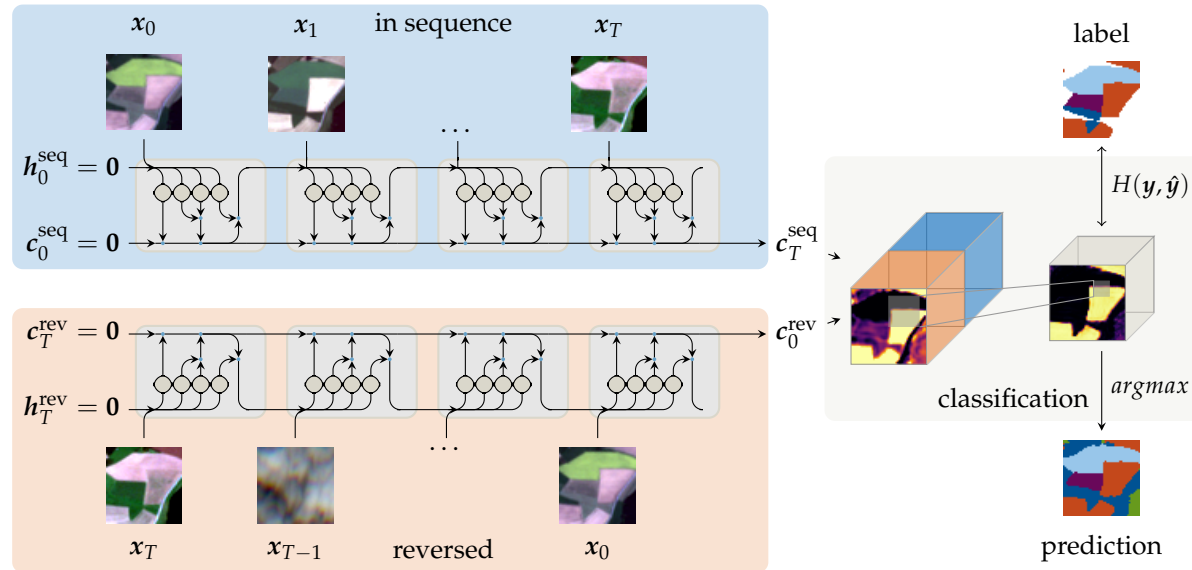


Figure 3. Schematic illustration of our proposed bidirectional sequential encoder network. The input sequence $\mathbf{x} \in \{\mathbf{x}_0, \dots, \mathbf{x}_T\}$ of observations $\mathbf{x}_t \in \mathbb{R}^{h \times w \times d}$ is encoded to a representation $\mathbf{c}_T = [\mathbf{c}_T^{\text{seq}} \parallel \mathbf{c}_0^{\text{inv}}]$. The observations are passed in sequence (seq) and reversed (rev) to the encoder in order to eliminate bias towards recent observations. The concatenated representation of both passes \mathbf{c}_T is then projected to softmax-normalized feature maps for each class using a convolutional layer.

a constant value and consequently ignored at the iterative encoding step. Observations are passed in *sequence* (*seq*) and *reversed* (*rev*) to the encoder while sharing weights between both passes. The initial cell states $\mathbf{c}_0^{\text{seq}}, \mathbf{c}_T^{\text{rev}} \in \mathbb{R}^{h \times w \times r}$ and output $\mathbf{h}_0^{\text{seq}}, \mathbf{h}_T^{\text{rev}} \in \mathbb{R}^{h \times w \times r}$ are initialized with zeros, and the number of cells r is treated as network hyper-parameter. The concatenated final state $\mathbf{c}_T = [\mathbf{c}_T^{\text{seq}} \parallel \mathbf{c}_0^{\text{inv}}]$ represents classification-relevant features of the entire sequence. Finally, these states are passed to a convolutional layer for classification, which reduces the feature depth from $2r$ to the number of classes n and *softmax*-normalizes the values to activations per class, which can be interpreted as confidences. In the classification layer, a *convolution* with a kernel size of k_{class} is followed by batch normalization and a *leaky relu* [34] or *relu* [35] non-linear activation function.

At each training step, the *cross-entropy* loss

$$H(\hat{\mathbf{y}}, \mathbf{y}) = - \sum_i \hat{y}_i \log(y_i) \quad (1)$$

between the predicted activations $\hat{\mathbf{y}}$ and a one-hot representation of the *ground truth* labels \mathbf{y} evaluates the prediction quality. Consequently, based the loss objective function and the Adam optimizer [36], gradients are back-propagated through the network layers and adjust the model weights.

Tunable hyper-parameters are the number of recurrent cells r and the sizes of the convolutional kernel k_{rnn} and the classification kernel k_{class} . Using this convolutional layer instead of a fully-connected layer for classification, our approach is fully-convolutional. Hence, the model weights are independent of spatial dimensions of the input and the size of inferred tiles can be changed without retraining the model. However, the perceptive field of the classification is solely determined by the kernel sizes k_{rnn} and k_{class} .

4. Dataset

For the evaluation of our approach, we defined a large area of interest (AOI) of $102 \text{ km} \times 42 \text{ km}$ north of Munich, Germany. To ensure dataset independence, while maintaining similar class

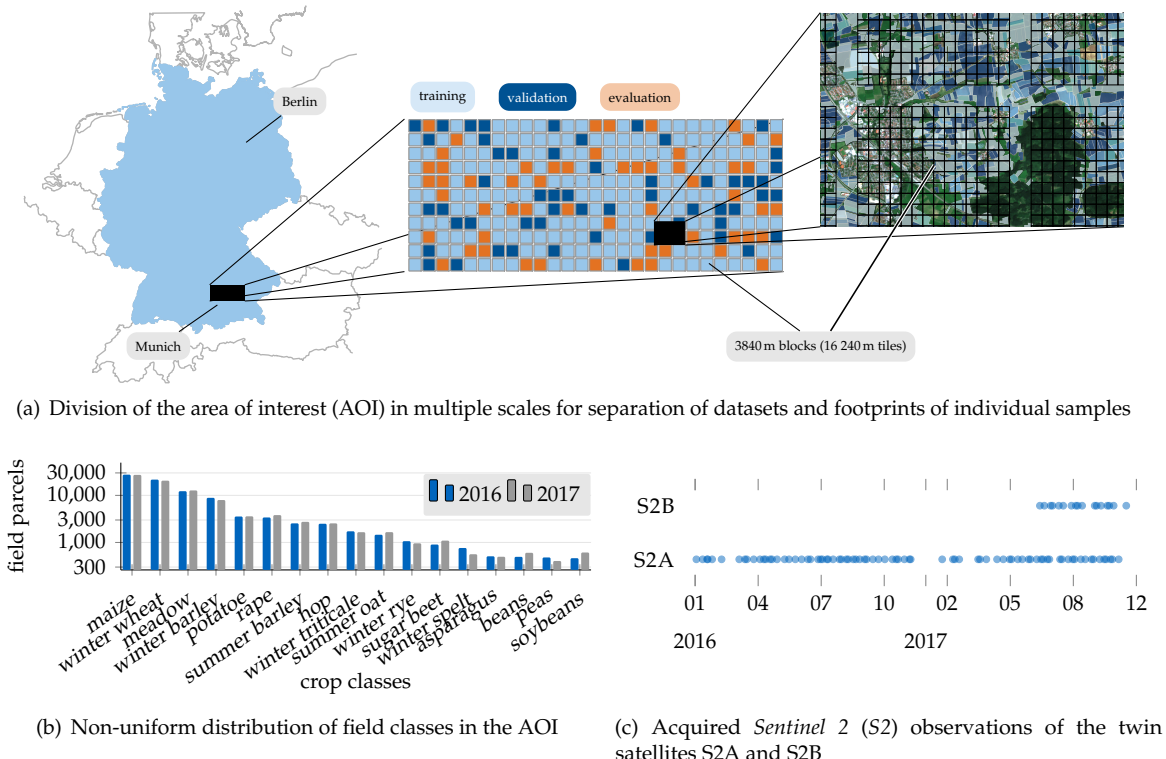


Figure 4. Information of the area of interest containing location, division schemes, class distributions and dates of acquired satellite imagery.

distributions, we subdivided the AOI further into squared blocks $3.84 \text{ km} \times 3.84 \text{ km}$ (multiples of 240 m and 480 m). These blocks were then randomly assigned to partitions for network training, hyper-parameter validation, and model evaluation. This was done in a ratio of 4:1:1 and is methodically similar to previous work [24]. An overview of the AOI at multiple scales is shown at Figure 4(a). The spatial border of single samples x are determined by tile-grids of 240 m and 480 m . Compared to previous work, we automatized and simplified the data sampling, as no additional cloud classes were required and atmospherically uncorrected *top-of-atmosphere* (TOA) reflectance values were passed to the network. Harmonizing the *ground sampling distances* (GSDs) of the *Sentinel 2* (S2) bands, we *bilinearly* interpolated the 20 m and 60 m bands to 10 m . To provide additional temporal meta information, the *year* and *day-of-year* of the individual observations were added as matrices to the input tensor. Hence, the input feature depth $d = 15$ is composed of four 10 m (B4, B3, B2, B8), six 20 m (B5, B6, B7, B8A), and three 60 m (B1, B11, B12) bands combined with *year* and *day-of-year*.

With ground truth labels of two vegetative growth seasons 2016 and 2017 available, we gathered 274 (108 in 2016; 166 in 2017) *Sentinel 2* products at 98 (46 in 2017; 52 in 2017) observation dates between 3rd January, 2016 and 15th November, 2017. The obtained time series represents all available S2 products labeled with cloud coverage less than 80%.

Ground truth information was provided by the *Bavarian Ministry of Food, Agriculture and Forestry* (StMELF) in form of geometry and semantic labels of 137 k field parcels. Information of the cultivated crops was provided from the individual farmers to the ministry in the scope of the European crop subsidy program. From approximately 200 distinct field labels, we selected and aggregated 17 classes, of which field parcels occurred at least 400 times in the AOI. With modern agriculture, centered around few predominant crops, the distribution of classes is not uniform, as can be observed from Figure 4(b). This non-uniform class distribution is generally not optimal for classification and evaluation of the results. For instance, the overall accuracy metrics may be skewed towards classes of high frequency.

However, non-uniform class distributions are common to EO applications and inherent to many LULC labels.

5. Results

5.1. Internal Network Activations

In Section 3.1, we gave an overview of the functionality of recurrent layers and discussed the property of LSTM state vectors $c_t \in \mathbb{R}^{h \times w \times r}$ to encode sequential information over a series of observations. The cell state is updated by internal gates $i_t, j_t, f_t \in \mathbb{R}^{h \times w \times r}$, which in turn are calculated based on previous cell output h_{t-1} and cell state c_{t-1} (see Table 1). In Figure 5, we visualized the activations of these tensors over the temporal series of observations. The LSTM network, on which these activations are extracted, was trained on $24 \text{ px} \times 24 \text{ px}$ tiles with $r = 256$ recurrent cells and $k_{\text{rnn}} = k_{\text{class}} = 3 \text{ px}$. For better visibility, we inferred the network with tiles of height h and width w of 48 px . Experiments with input size of 24 px show similar results and are included in the complementary material to this work. At the first row, the input tensor $x_t \in \mathbb{R}^{h=48 \times w=48 \times d=15}$ is represented by a normalized RGB image. For visualization purposes, we normalized the RGB images by 4σ standard deviation of each band. Further rows show the activations of input gate i_t^i , modulation gate j_t^i , forget gate f_t^i , and cell state c_t^i at three selected recurrent cells, which are denoted by the raised index $i \in \{3, 22, 47\}$. As described in Section 3.2, the final cell state is used by the softmax-classification layer to produce activations for each class.

One can observe that over the sequence of observations, the details of structures visible at cell state increased gradually. This may be interpreted as additional information written to the cell state. Furthermore, it appeared that the structures visible at the cell states generally resembled shapes, which were visible in cloud-free RGB images (e.g., $c_{t=15}^{(3)}$ or $c_{t=28}^{(22)}$). Some cells (e.g., cell 3 or cell 22) changed their activations gradually over the span of multiple observations, while others (e.g., 47) seemed to change more frequently. Looking further at internal gate activations, one may interpret low (dark) forget gate f activations as forgetting information from the previous state. As iterated before, the input and modulation gates j, i control the degree of new information written to the cell state. While values of the input gate are scaled between zero and one, the modulation gate $j \in [-1, 1]$ determines the sign of change. We found that for many cells (e.g., cell 3 or cell 22) the activations of internal gated were difficult to associate with visible events in the current input. However, some cells (e.g., 47) were visually interpretable, as the shape of clouds, visible in the RGB image, was projected to in the internal activations. At cloudy observations, the input gate (e.g., $i_t^{(47)}$) seems to approach zero either over the entire tile (e.g., $t = \{10, 18, 19, 36\}$) or at patches of cloudy pixels (e.g., $t = \{11, 13, 31, 33\}$). At some observations (e.g., $t = \{13, 31, 32\}$) the modulation gate $j_t^{(47)}$ additionally changed the sign at cloudy and not-cloudy pixels.

Similar to this experiment, Karpathy [37] evaluated cell activations for the task of text summarization and could associate a small number of cells to a set of distinct tasks. In that context, we suspect that the grammar of crop-characteristic phenological changes are encoded in the network weights. Furthermore, we found cells which are sensible to cloud coverage and are likely to be used in combination with other cells within the network for discriminating classification relevant from non-classification relevant observations. Thus, we are confident that our network has internalized a cloud-filtering scheme by learning that cloudy observations, which are expressed by a sudden increase in reflectance, do not contribute to the classification task.

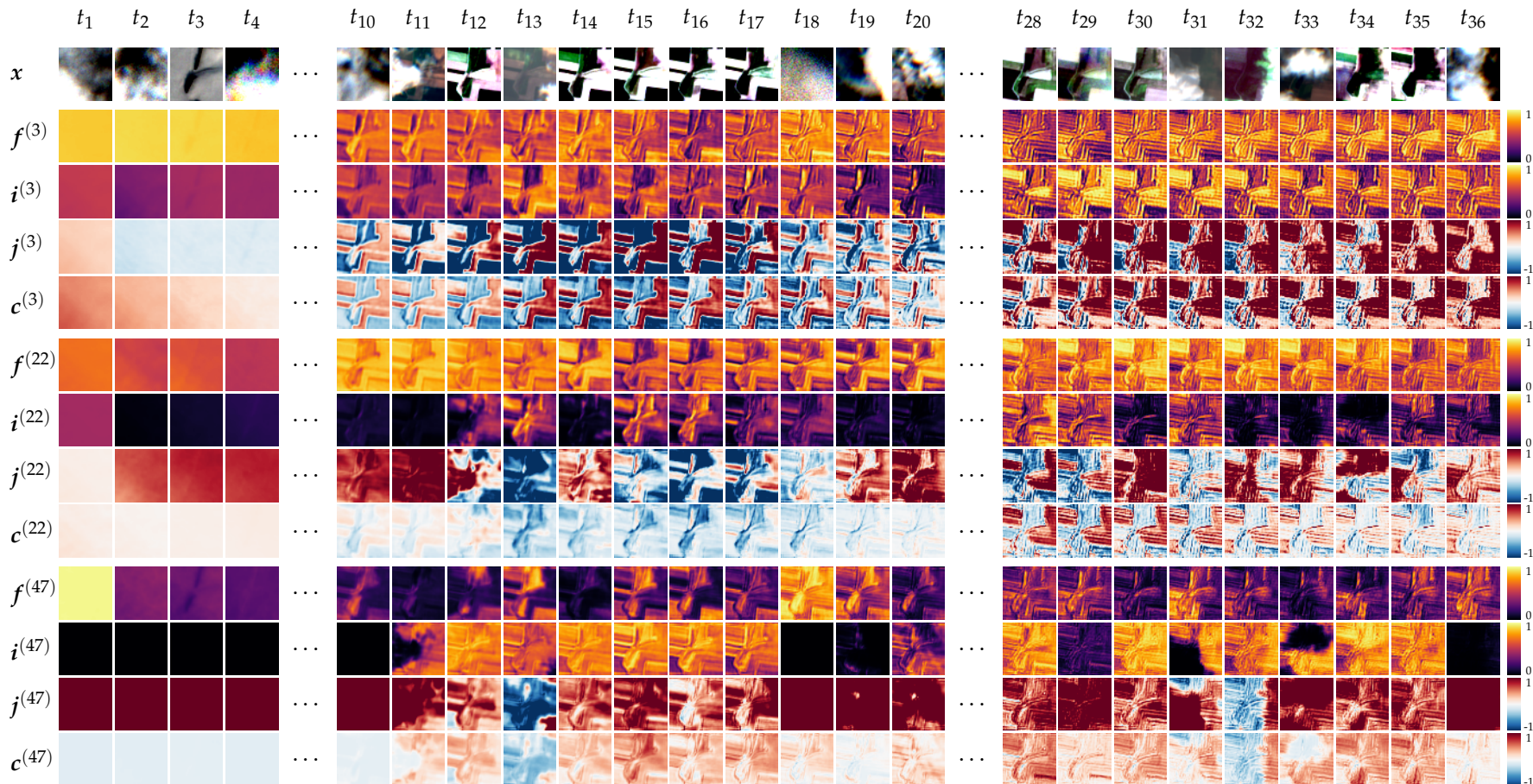


Figure 5. Activations of input gate $i^{(i)}$, forget gate $f^{(i)}$, modulation gate $j^{(i)}$ and cell state $c^{(i)}$ at three (of $r = 256$) selection cells $i \in \{3, 22, 47\}$ given the current input x_t over the sequence of observations $t = \{1, \dots, 36\}$. The detail of features at the cell states increases gradually, which indicates the aggregation of information over the sequence. While likely most cells contribute to the classification decision, only some cells are visually interpretable with regard to the current input x_t . One visually interpretable cell is $i = 47$, which has learned cloud masking and filtering, as input and modulation gates clearly show different activations on cloudy and non-cloudy observations.

Table 2. Pixel-wise accuracies of the trained convolutional GRU sequential encoder network after training over 60 epochs on data of both growth seasons.

Class	Year							
	2016				2017			
	Precision	Recall	f-Measure	#Pixels	Precision	Recall	f-Measure	#Pixels
sugar beet	95	78	85	59k	89	79	83	94k
summer oat	86	68	76	36k	64	63	63	38k
meadow	91	86	88	233k	88	85	87	242k
rape	95	90	93	125k	96	96	96	114k
hop	96	87	92	51k	93	75	83	53k
winter spelt	55	81	66	38k	75	47	58	31k
winter triticale	69	56	62	65k	62	57	60	64k
beans	92	87	90	27k	93	63	75	28k
peas	93	71	80	9k	61	41	49	6k
potato	91	88	90	125k	95	74	83	140k
soybeans	98	80	88	21k	76	80	78	26k
asparagus	89	79	84	20k	82	77	79	19k
winter wheat	88	93	90	806k	90	95	92	783k
winter barley	95	87	91	258k	93	92	92	255k
winter rye	86	47	61	43k	77	62	69	30k
summer barley	88	83	85	73k	78	88	83	91k
maize	92	96	94	920k	92	97	94	876k
weight. avg	90	90	90		89	90	89	

5.2. Quantitative Classification Evaluation

We trained networks of our sequential encoder structure (see Section 3.2) with bidirectional convolutional LSTM and GRU cells with $r \in \{128, 256\}$ recurrent cells. Kernel sizes of $k_{\text{rnn}} = k_{\text{class}} = 3$ were used for the evaluation, since previous tests with larger kernel sizes showed similar accuracies, while a larger number of weights prolonged training time. For these initial experiments, we predominantly tested network variants with $r = 128$ recurrent cells, as these are faster to train. However, for the final evaluation, we used $r = 256$ recurrent cells, since we found that these achieved slightly better results at the cost of more weights and longer training. The training of convolutional GRU and LSTM networks was performed on a P100 GPU for 60 epochs (3.51m 24 px \times 24 px tiles seen) and took 58 h and 51 h, respectively. In terms of data augmentation, we randomly sampled 30 of all available 46 (2016) and 52 (2017) observations. However, the random sampling maintained the sequence of observations. For all our tests, we found that the performance of LSTM and GRU networks was similar. However, fewer weights of GRU cells allowed using a slightly larger batch size of 32 samples compared to 28 samples of LSTM, which lead to a 7 h faster training compared to the LSTM variant. Thus, we decided to report evaluation results of the GRU network in this work. We trained the network on tiles of 24 px. Pixels without ground truth had been masked since we decided not to include a rejection class. Hence, we did not punish the network for false predictions at pixels containing structures which are not represented in our set of classes (e.g., urban structures, forests, water bodies).

Accuracies per class for both years are shown at Table 2. The best and worst metrics are additionally emphasized by boldface. In general, the pixel-averaged achieved precision, recall, and f-score accuracies were consistent over both years and ranged between 89% and 90%. However, the classification accuracies per class varied largely between f-scores of 61% (rye) and 94% (maize) in 2016 and 58% (spelt) to 96% (rape). Naturally, frequent classes (e.g., maize, meadow) have been more confidently classified than less frequent classes (e.g., peas, summer oat, winter spelt, winter triticale). Nonetheless, this relation has exceptions, as the least frequent class, peas, performed relatively well at

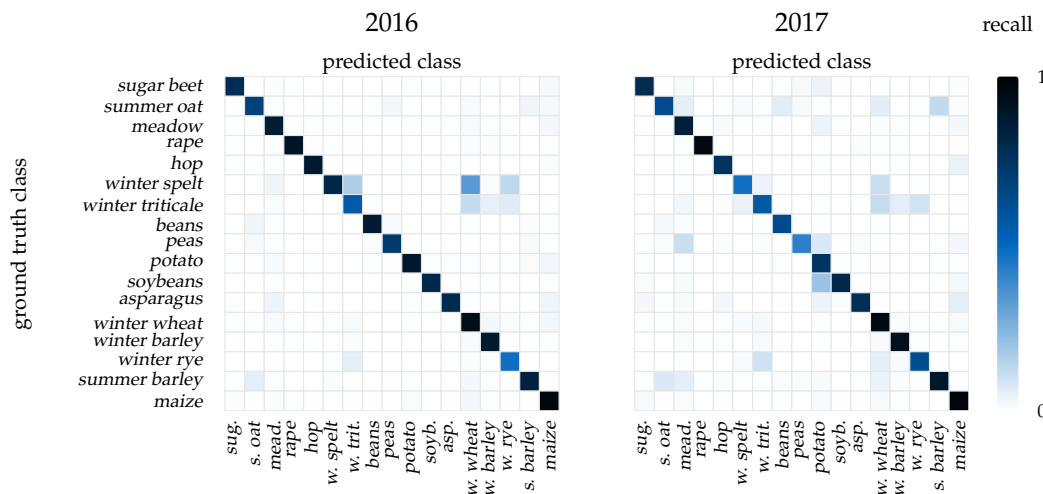


Figure 6. Confusion matrix of the trained convolutional GRU network on data of the growth seasons 2016 and 2017. While the confusion of some classes was consistent over both growth seasons (e.g., *winter triticale* to *winter wheat*), other classes are classified at different accuracies at consecutive years (e.g., *winter barley* to *winter spelt*).

data of 2016 and other less frequent classes (e.g., *asparagus*, *hop*) showed good performances despite their underrepresentation in the dataset.

Further, we identified three types of confusions between classes in Figure 6. Some crops were confused with each other likewise, which is indicated by a diagonal symmetric structure at both years. Examples of this were *triticale* and *rye*, or *oat* and *summer barley*. A second *asymmetrical* confusion occurred, when—consistent over both years—one class was confused with another, but not *vice-versa*. This resulted in a asymmetric appearance which is visible in both confusion matrices. Relations of this type were *barley* confused with *triticale*, *triticale* with *spelt*, or *wheat* confused with *triticale* and *spelt*. Naturally, we expected some classes to have a more similar spectral, or temporal characteristic, which would complicate classes separation. Since these confusions were consistent over both years, it is likely that these are caused by characteristics of the respective crop types. Furthermore, these confusions are to some degree inherent to any classifier, generally less frequent, and were consistent over both growth periods.

More dominantly, many errors in classification were not consistent over the two growth seasons. For instance, confusions occurring only in the 2017 growth seasons are: *soybeans* with *potato* or *peas* with *meadow* and *potato*. As reported in Table 2, *peas* have been classified well in 2016, but performed worst of all classes at 2017, due to aforementioned confusions with *meadow* and *potato*. Apparently, unique to one growth season, external and not crop-type related factors had a negative influence on classification accuracies. One of these might be the variable onset of phenological events, which we indirectly observed by the change of reflectance over the sequence of observations. These events are influenced by local weather and sun exposure which may vary over large regional scales or at different seasons. To account for these factors, additional meteorological information could be introduced to the classifier, as done by Foerster *et al.* [9], who extracted phenologically corrected features using additional agro-meteorological data. In a deep learning framework, this may be realized by augmenting the input feature matrix with available meteorological of regional information. An end-to-end trained network would likely extract classification relevant features automatically. This is similar to our addition of day-of-year and year of the respective observation. However, the effect of this additionally provided information still remains to be evaluated.

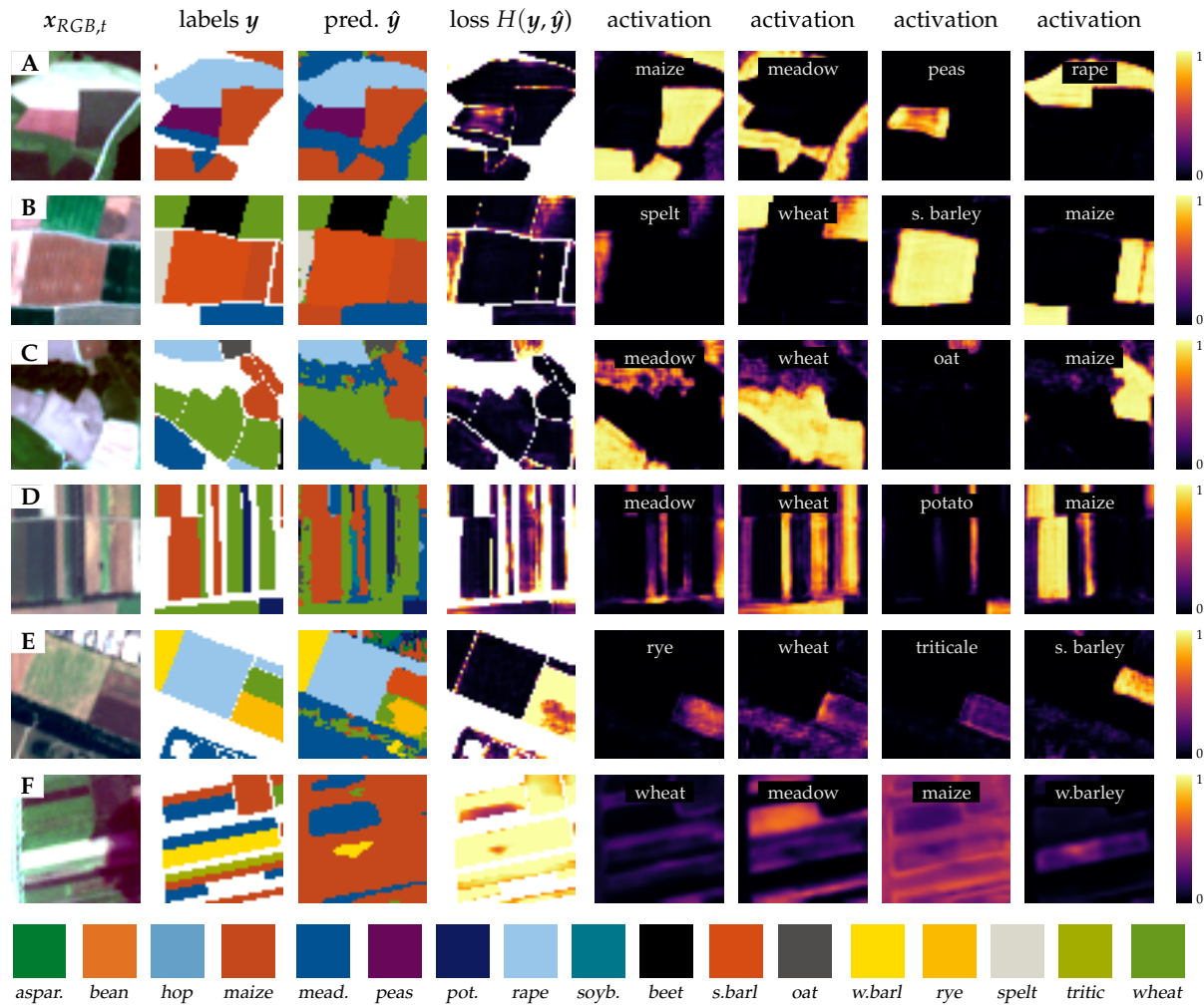


Figure 7. Qualitative results of the convolutional GRU sequential encoder. Examples A–D show good classification results, while at example E the network misclassified one *maize* field with high confidence and was uncertain between *wheat*, *meadow* and *maize* for a second field. At example F most pixels are misclassified. However, the class activations indicate uncertain classification decisions.

5.3. Qualitative Classification Evaluation

For the qualitative evaluation, we used the same network as previously, but inferred it with 48 px tiles from the evaluation dataset of 2017. Figure 7 shows a series of good (A–D) and bad (E, F) classification examples. At the first column, band-normalized RGB images from one selected cloud-free observation $x_{RGB,t}$ represent the input feature vectors x . Further columns show the available ground truth labels y , predictions \hat{y} , and the cross-entropy loss $H(y, \hat{y})$ between the former. Additionally, four selected softmax-normalized class activations are displayed in the last columns. These activations can, to some degree, be interpreted as network confidences for the classification decision of the respective class. The prediction, as the argument of the maximum class activation, resembles the most confident class at each pixel. In contrast, the cross-entropy loss is calculated based on all activations which may increase the loss at correctly predicted classes even if the pixel is correctly predicted. This can be observed at fields of several examples: *peas* in example A, *spelt* in example B, and *oat* in example C. However, at these examples, most classifications were generally accurate which is indicated by spatially distinct activations with defined boundaries and class-activations which saturated to one. Example D shows a tile with a series narrow fields of only few pixels in width. Two thin *wheat* and

maize fields have been classified correctly. However, some errors occurred on the southern end of an adjacent *potato* field, as indicated by the loss map. It seems that the network was able to resolve changes of high spatial frequency and did not implicitly smooth the class activations.

Two misclassified fields are shown in example E. The upper *wheat* field has been confidently misclassified to *summer barley*, while underneath, the classification at a second *rye* field was uncertain between *rye*, *wheat*, and *triticale*, as can be seen on the levels of activations for each crop. While *triticale*, as the least activated class, was not present in the predictions, the mixture of *rye* and *wheat* is clearly visible on the map of predictions.

Example F shows a mostly misclassified tile. While some patches of *meadow* and *winter barley* were correctly predicted, the activations of these classes were, compared to previous examples, generally more blurred and of lower amplitude. Similar to example D, the predominantly activated classes are also the most frequent in the dataset. In fact, the entire region around the displayed tile seemed to be classified poorly. This region was located on the north-west border of the AOI. As previously iterated, phenological events are variable over large spatial distances or multiple seasons. Without information of spatial locality, the network likely approximated an averaged phenological model for each crop over the entire region. This model might have implicitly encoded region-dependent variables, such as weather, precipitation, or sun exposure. Hence, the trained model might not be representative for the growth behavior at the outer borders of the AOI, which would result in inferior classification performance. Introducing additional regional information to the model might potentially alleviate these issues by conditioning the learned models to the respective regions.

6. Discussion

Today, earth observation data is acquired at high frequency and at low cost. From an information theoretical perspective, additional data should aid classification. However, as referred to in Section 1, this large amount of data requires methods which are able to utilize this gain of information and, optimally, are scalable with regard to further observations of a larger area of interest. Existing approaches in multi-temporal *earth observation* (EO) tasks often use multiple separate processing steps, such as preprocessing, feature extraction, and classification, as summarized by Ünsalan and Boyer [38]. Generally, these steps require manual supervision or the selection of additional parameters. In Table 3, we gathered multi-temporal crop classification approaches and compare these on several categories, such as the source of data, used preprocessing steps, extracted features, applied classifier, achieved accuracy, and the number of classes. Aside from data processing limitations, the cost of data acquisition is an additional barrier for scalability at multi-temporal applications, as multiple, potentially expensive, satellite images are required. At one side, commercial satellites, such as *RapidEye* (RE), *Satellite Pour l'Observation de la Terre* (SPOT), or *QuickBird* (QB), provide images at best available spatial resolution and are acquired at fast intervals. However, predominantly inexpensive sensors, such as *Landsat* (LS), *Sentinel 2* (S2), *Moderate-resolution Imaging Spectroradiometer* (MODIS), or *Advanced Spaceborne Thermal Emission and Reflection Radiometer* (ASTER), are effectively applicable for large-scale multi-temporal applications at reasonable costs. Many approaches extract statistical features from spectral indices, such as *normalized difference vegetation index* (NDVI), *normalized difference water index* (NDWI), or *enhanced vegetation index* (EVI), which are used to describe the underlying crop-specific phenological model. Commonly *decision trees* (DTs) or *random forests* (RFs) are used for classification. The exclusive use of spectral indices simplifies the task of feature extraction, however, only utilizes a small number of available spectral information (predominantly *red* and *near-infrared*). Thus, methods that utilize all reflectance measurements, either at *top-of-atmosphere* (TOA), or atmospherically corrected to *bottom-of-atmosphere* (BOA), are favorable, since all potential spectral information can be extracted.

In general, a direct numerical comparison of classification accuracies is difficult, since these measures should be seen in the context of quantity of evaluated samples, the extent of evaluated area, and the number of classified categories. However, the approaches of Siachalou *et al.* [14] and Hao *et al.* [12] achieve good classification accuracies on a smaller set of classes. Hao *et al.* [12] use a

Table 3. Overview over recent approaches for crop classification.

Approach	Details					
	Sensor	Preprocessing	Features	Classifier	Accuracy	# Classes
this work	S2	none	TOA reflect.	ConvRNN	90	17
Rußwurm and Körner [24, 2017]	S2	atm. cor. (SEN2COR)	BOA reflect.	RNN	74	18
Siachalou <i>et al.</i> [14, 2015]	LS, RE	geometric correction, image registration	TOA reflect.	HMM	90	6
Hao <i>et al.</i> [12, 2015]	MODIS	image reprojection, atm. cor. [39]	statistical phen. features	RF	89	6
Conrad <i>et al.</i> [11, 2014]	SPOT, RE, QB	segmentation, atm. cor. [39]	vegetation indices	OBIA+RF	86	9
Foerster <i>et al.</i> [9, 2012]	LS	phen. normalization, atm. cor. [39]	NDVI statistics	DT	73	11
Peña-Barragán <i>et al.</i> [40, 2011]	ASTER	segmentation, atm. cor. [41]	vegetation indices	OBIA+DT	79	13
Conrad <i>et al.</i> [10, 2010]	SPOT ASTER	segmentation, atm. cor. [39]	vegetation indices	OBIA+DT	80	6

random forest classifier on phenological features, which have been extracted from NDVI and NDWI time series of MODIS data. Their results show that good classification accuracies with traditional feature extraction and classification methods can be achieved if data of sufficient temporal resolution is available. However, the large spatial resolution (500 m) of the MODIS sensor limits the application to areas of large homogeneous regions. In contrast, Siachalou *et al.* [14] report good accuracies on small fields with an *hidden Markov model* (HMM) approach. They use on a temporal series of four Landsat images and one RapidEye image. In general, the use of *hidden Markov models* (HMMs) and *conditional random fields* (CRFs) [15] is methodically closer to our recurrent deep learning approach since the phenological model is approximated with an internal chain of hidden states. However, these methods might not be applicable for long temporal series, since it is assumed that only one previous state contains classification-relevant information.

Overall, Table 3 shows that our proposed network can achieve state-of-the-art classification accuracy with a large number of classes. Furthermore, the *Sentinel 2* (S2) data of non-atmospherically corrected *top-of-atmosphere* (TOA) values can be acquired easily and does not require further preprocessing. Compared to our previous work, we were able to process larger tiles by using convolutional recurrent cells with only a single recurrent encoding layer. Moreover, we did neither require atmospheric correction nor additional cloud classes, since one classification decision is derived from the entire sequence of observations.

7. Conclusion

Building on previous work [24], we proposed an automated end-to-end approach for multi-temporal classification which achieved state-of-the-art accuracies on crop classification tasks with a large number of crop classes. Furthermore, the proposed network had been trained on not atmospherically corrected data without prior cloud-filtering. In traditional approaches, multi-temporal cloud detection algorithms [42] utilize the sudden positive change in reflectivity at cloudy pixels and achieve better results than other traditional mono-temporal remote sensing classifiers, as pointed out by a recent comparison [43]. Results of this work indicate that these cloud identification characteristics can be learned automatically along with the classification in an end-to-end scheme. By visualizing

internal gate activations in our network at Section 5.1, we found several recurrent cells which have been trained to internally mask cloud pixels.

In Sections 5.2 and 5.3, we further evaluated the classification results quantitatively and qualitatively. Based on several findings, we derived that the network has approximated a discriminative crop-specific phenological model based on a raw series of TOA S2 observations. However, inconsistent classification errors between both growth seasons and worse classification performance at the *area of interest (AOI)* border suggest that seasonal and regional environmental conditions might have been implicitly integrated in the encoded phenological model. In future work, additional regional information may possibly help to condition the phenological model on the respective region. Nevertheless, we hope that our results encourage the research community to utilize the temporal domain for their applications. In that regard, we plan to publish the TENSORFLOW source code of our network along with the evaluations and experiments from this work.

Supplementary Materials: The code of the network and further material will be published at <http://www.lmf.bgu.tum.de/research/mlcc>.

Acknowledgments: We would like to thank the *Bavarian Ministry of Food, Agriculture and Forestry (StMELF)* for providing ground truth data in excellent semantic and geometric quality. Furthermore, we thank the *Leibnitz Supercomputing Centre (LRZ)* for providing access to computational resources, such as DGX-1 and P100 servers and NVIDIA for providing one TITAN X GPU.

1. Odenweller, J.B.; Johnson, K.I. Crop identification using Landsat temporal-spectral profiles. *Remote Sensing of Environment* **1984**, *14*, 39–54.
2. Reed, B.C.; Brown, J.F.; VanderZee, D.; Loveland, T.R.; Merchant, J.W.; Ohlen, D.O. Measuring Phenological Variability from Satellite Imagery. *Journal of Vegetation Science* **1994**, *5*, 703–714.
3. Bahdanau, D.; Cho, K.; Bengio, Y. Neural Machine Translation by Jointly Learning to Align and Translate. *Arxiv* **2014**, [\[1409.0473\]](#).
4. Rush, A.; Chopra, S.; Weston, J. A Neural Attention Model for Sentence Summarization. *Arxiv* **2017**.
5. Shen, S.; Liu, Z.; Sun, M. Neural Headline Generation with Minimum Risk Training. *Arxiv* **2016**, [\[arXiv:1604.01904v1\]](#).
6. Nallapati, R.; Zhou, B.; dos Santos, C.N.; Gulcehre, C.; Xiang, B. Abstractive Text Summarization Using Sequence-to-Sequence RNNs and Beyond. *Arxiv* **2016**, [\[1602.06023\]](#).
7. Sutskever, I.; Vinyals, O.; Le, Q.V. Sequence to Sequence Learning with Neural Networks. *Arxiv* **2014**, [\[1409.3215\]](#).
8. Chorowski, J.; Bahdanau, D.; Serdyuk, D.; Cho, K.; Bengio, Y. Attention-based models for speech recognition. NIPS, 2015, pp. 577–585, [\[1506.07503\]](#).
9. Foerster, S.; Kaden, K.; Foerster, M.; Itzerott, S. Crop type mapping using spectral-temporal profiles and phenological information. *Computers and Electronics in Agriculture* **2012**, *89*, 30–40.
10. Conrad, C.; Fritsch, S.; Zeidler, J.; Rücker, G.; Dech, S. Per-Field Irrigated Crop Classification in Arid Central Asia Using SPOT and ASTER Data. *Remote Sensing* **2010**, *2*, 1035–1056.
11. Conrad, C.; Dech, S.; Dubovik, O.; Fritsch, S.; Klein, D.; Löw, F.; Schorcht, G.; Zeidler, J. Derivation of temporal windows for accurate crop discrimination in heterogeneous croplands of Uzbekistan using multitemporal RapidEye images. *Computers and Electronics in Agriculture* **2014**, *103*, 63–74.
12. Hao, P.; Zhan, Y.; Wang, L.; Niu, Z.; Shakir, M. Feature Selection of Time Series MODIS Data for Early Crop Classification Using Random Forest: A Case Study in Kansas, USA. *Remote Sensing* **2015**, *7*, 5347–5369.
13. Peña-Barragán, J.M.; Ngugi, M.K.; Plant, R.E.; Six, J. Object-based crop identification using multiple vegetation indices, textural features and crop phenology. *Remote Sensing of Environment* **2011**, *115*, 1301–1316.
14. Siachalou, S.; Mallinis, G.; Tsakiri-Strati, M. A Hidden Markov Models Approach for Crop Classification: Linking Crop Phenology to Time Series of Multi-Sensor Remote Sensing Data. *Remote Sensing* **2015**, *7*, 3633–3650.

15. Hoberg, T.; Rottensteiner, F.; Feitosa, R.Q.; Heipke, C. Conditional random fields for multitemporal and multiscale classification of optical satellite imagery. *IEEE Transactions on Geoscience and Remote Sensing (TGRS)* **2015**, *53*, 659–673.
16. Zhu, X.X.; Tuia, D.; Mou, L.; Xia, G.S.; Zhang, L.; Xu, F.; Fraundorfer, F. Deep learning in remote sensing: a review. *Arxiv* **2017**, [\[1710.03959\]](https://arxiv.org/abs/1710.03959).
17. Hu, F.; Xia, G.S.; Hu, J.; Zhang, L. Transferring Deep Convolutional Neural Networks for the Scene Classification of High-Resolution Remote Sensing Imagery. *Remote Sensing* **2015**, *7*, 14680–14707.
18. Scott, G.J.; England, M.R.; Starms, W.A.; Marcum, R.A.; Davis, C.H. Training Deep Convolutional Neural Networks for Land-Cover Classification of High-Resolution Imagery. *IEEE Geoscience and Remote Sensing Letters (GRSL)* **2017**, *14*, 549–553.
19. Makantasis, K.; Karantzalos, K.; Doulamis, A.; Doulamis, N. Deep Supervised Learning for Hyperspectral Data Classification through Convolutional Neural Networks. *Geoscience and Remote Sensing Symposium (IGARSS)*. IEEE, 2015, pp. 4959–4962.
20. Castelluccio, M.; Poggi, G.; Sansone, C.; Verdoliva, L. Land Use Classification in Remote Sensing Images by Convolutional Neural Networks. *arXiv preprint arXiv:1508.00092* **2015**, pp. 1–11, [\[1508.00092\]](https://arxiv.org/abs/1508.00092).
21. Jia, X.; Khandelwal, A.; Nayak, G.; Gerber, J.; Carlson, K.; West, P.; Kumar, V. Incremental Dual-memory LSTM in Land Cover Prediction. *23rd ACM SIGKDD International Conference on Knowledge Discovery and Data Mining*, 2017, pp. 867–876.
22. Braakmann-Folgmann, A.; Roscher, R.; Wenzel, S.; Uebbing, B.; Kusche, J. Sea Level Anomaly Prediction using Recurrent Neural Networks. *Arxiv* **2017**, [\[1710.07099\]](https://arxiv.org/abs/1710.07099).
23. Sharma, A.; Liu, X.; Yang, X. Land Cover Classification from Multi-temporal, Multi-spectral Remotely Sensed Imagery using Patch-Based Recurrent Neural Networks. *Arxiv* **2017**, [\[1708.00813\]](https://arxiv.org/abs/1708.00813).
24. Rußwurm, M.; Körner, M. Temporal Vegetation Modelling using Long Short-Term Memory Networks for Crop Identification from Medium-Resolution Multi-Spectral Satellite Images. *IEEE/ISPRS Workshop on Large Scale Computer Vision for Remote Sensing Imagery (EarthVision)*, 2017, Proceedings of the IEEE Conference on Computer Vision and Pattern Recognition (CVPR) Workshops.
25. Hochreiter, S.; Schmidhuber, J. Long Short-Term Memory. *Neural Computation* **1997**, *9*, 1735–1780.
26. Cho, K.; van Merriënboer, B.; Gulcehre, C.; Bahdanau, D.; Bougares, F.; Schwenk, H.; Bengio, Y. Learning Phrase Representations using RNN Encoder-Decoder for Statistical Machine Translation. *arXiv preprint arXiv:1406.1078* **2014**, [\[1406.1078\]](https://arxiv.org/abs/1406.1078).
27. Graves, A.; Wayne, G.; Danihelka, I. Neural Turing Machines. *Arxiv* **2014**, [\[1410.5401\]](https://arxiv.org/abs/1410.5401).
28. Siegelmann, H.; Sontag, E. On the Computational Power of Neural Nets. *Journal of Computer and System Sciences* **1995**, *50*, 132–150.
29. Rafal, J.; Wojciech, Z.; Ilya, S. An Empirical Exploration of Recurrent Network Architectures. *Proceedings of the 32nd International Conference on International Conference on Machine Learning*, 2015, Vol. 7, pp. 2342–2350, [\[1512.03385\]](https://arxiv.org/abs/1512.03385).
30. Hochreiter, S.; Bengio, Y.; Frasconi, P.; Schmidhuber, J. Gradient flow in recurrent nets: the difficulty of learning long-term dependencies. *A Field Guide to Dynamical Recurrent Networks* **2001**, pp. 237–243, [\[arXiv:1011.1669v3\]](https://arxiv.org/abs/1011.1669v3).
31. Yoshua, B.; Patrice, S.; Paolo, F. Learning long-term dependencies with gradient descent is difficult. *IEEE transactions on neural networks* **1994**, *5*, 157–166.
32. Shi, X.; Chen, Z.; Wang, H.; Yeung, D.Y.; Wong, W.K.; Woo, W.C. Convolutional LSTM Network: A Machine Learning Approach for Precipitation Nowcasting. *Arxiv* **2015**.
33. Gehring, J.; Auli, M.; Grangier, D.; Yarats, D.; Dauphin, Y.N. Convolutional Sequence to Sequence Learning. *Arxiv* **2017**, [\[1705.03122\]](https://arxiv.org/abs/1705.03122).
34. Maas, A.L.; Hannun, A.Y.; Ng, A.Y. Rectifier Nonlinearities Improve Neural Network Acoustic Models. *Proceedings of the 30 th International Conference on Machine Learning* **2013**, *28*, 6.
35. Hahnloser R.; Sarpeshkar R.; Mahowald M A.; Douglas R. J.; Seung H. S.. Digital selection and analogue amplification coexist in a cortex-inspired silicon circuit. *Nature* **2000**, *405*, 947–951.
36. Kingma, D.P.; Ba, J.L. Adam: A Method for Stochastic Optimization. *ArXiv Preprint (1412.6980)* **2014**, [\[arXiv:1412.6980\]](https://arxiv.org/abs/1412.6980).
37. Karpathy, A. The unreasonable effectiveness of recurrent neural networks, 2015.

38. Ünsalan, C.; Boyer, K.L. Review on Land Use Classification. In *Multispectral Satellite Image Understanding: From Land Classification to Building and Road Detection*; Springer, 2011; pp. 49–64.
39. Richter, R. A spatially adaptive fast atmospheric correction algorithm. *International Journal of Remote Sensing* **1996**, *17*, 1201–1214.
40. Peña-Barragán, J.M.; Ngugi, M.K.; Plant, R.E.; Six, J. Object-based crop identification using multiple vegetation indices, textural features and crop phenology. *Remote Sensing of Environment* **2011**, *115*, 1301–1316.
41. Matthew, M.W.; Adler-Golden, S.M.; Berk, A.; Richtsmeier, S.C.; Levine, R.Y.; Bernstein, L.S.; Acharya, P.K.; Anderson, G.P.; Felde, G.W.; Hoke, M.P. Status of Atmospheric Correction using a MODTRAN4-Based Algorithm. SPIE proceeding. Algorithms for multispectral, hyperspectral, and ultra-spectral imagery VI, 2000, pp. 199–207.
42. Hagolle, O.; Huc, M.; Villa Pascual, D.; Dedieu, G. A multi-temporal method for cloud detection, applied to FORMOSAT-2, VENuS, LANDSAT and SENTINEL-2 images. *Remote Sensing of Environment* **2010**, *114*, 1747–1755.
43. Zupanc, A.S. Improving Cloud Detection with Machine Learning, 2017.



© 2018 by the authors. Licensee MDPI, Basel, Switzerland. This article is an open access article distributed under the terms and conditions of the Creative Commons Attribution (CC BY) license (<http://creativecommons.org/licenses/by/4.0/>).